JACS
JOURNAL OF THE AMERICAN CHEMICAL SOCIETY

Article

pubs.acs.org/JACS

Interplay between Size, Composition, and Phase Transition of Nanocrystalline Cr^{3+}-Doped $BaTiO_3$ as a Path to Multiferroism in Perovskite-Type Oxides

Ling Ju, Tahereh Sabergharesou, Kevin G. Stamplecoskie, Manu Hegde, Ting Wang, Nicole A. Combe, Hongyu Wu, and Pavle V. Radovanovic*

Department of Chemistry, University of Waterloo, 200 University Avenue West, Waterloo, Ontario, Canada N2L 3G1

Supporting Information

ABSTRACT: Multiferroics, materials that exhibit coupling between spontaneous magnetic and electric dipole ordering, have significant potential for high-density memory storage and the design of complex multistate memory elements. In this work, we have demonstrated the solvent-controlled synthesis of Cr^{3+}-doped $BaTiO_3$ nanocrystals and investigated the effects of size and doping concentration on their structure and phase transformation using X-ray diffraction and Raman spectroscopy. The magnetic properties of these nanocrystals were studied by magnetic susceptibility, magnetic circular dichroism (MCD), and X-ray magnetic circular dichroism (XMCD) measurements. We observed that a decrease in nanocrystal size and an increase in doping concentration favor the stabilization of the paraelectric cubic phase, although the ferroelectric tetragonal phase is partly retained even in ca. 7 nm nanocrystals having the doping concentration of ca. 5%. The chromium(III) doping was determined to be a dominant factor for destabilization of the tetragonal phase. A combination of magnetic and magneto-optical measurements revealed that nanocrystalline films prepared from as-synthesized paramagnetic Cr^{3+}-doped $BaTiO_3$ nanocrystals exhibit robust ferromagnetic ordering (up to ca. 2 μ_B/Cr^{3+}), similarly to magnetically doped transparent conducting oxides. The observed ferromagnetism increases with decreasing constituent nanocrystal size because of an enhancement in the interfacial defect concentration with increasing surface-to-volume ratio. Element-specific XMCD spectra measured by scanning transmission X-ray microscopy (STXM) confirmed with high spatial resolution that magnetic ordering arises from Cr^{3+} dopant exchange interactions. The results of this work suggest an approach to the design and preparation of multiferroic perovskite materials that retain the ferroelectric phase and exhibit long-range magnetic ordering by using doped colloidal nanocrystals with optimized composition and size as functional building blocks.

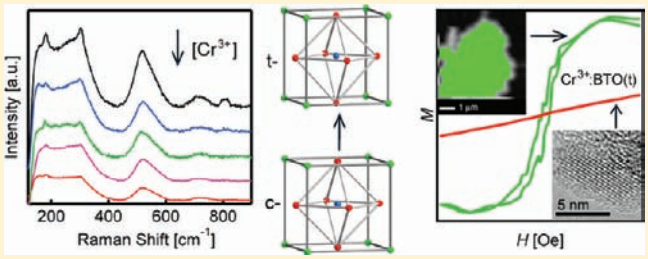

INTRODUCTION

The discoveries of new materials exhibiting a rare combination of magnetic and electric orderings, known as magnetoelectrics or multiferroics,[1,2] are of paramount importance for a deeper understanding of the interactions between electric polarization and magnetization in the solid state. The alignment of electric dipoles by using a magnetic field[3] or magnetic moments by applying a voltage[3,4] has been a long-pursued goal leading toward increasing the memory storage density and the design of multistate memory elements in which information can be stored using both electric and magnetic polarizations. Other potential applications include the fabrication of advanced memory media that could allow for writing the bits of information in the ferroelectric mode and reading them via a magnetic field generated through the magnetoelectric coupling, or vice versa. However, only few materials have shown an appreciable magnetoelectric effect, usually at temperatures well below room temperature.[5] This problem has been associated with chemical incompatibility of the two ordering mechanisms. Such an incompatibility can be illustrated in the case of the most widely used and best understood ferroelectrics: oxides with the perovskite crystal structure.

The complex oxide perovskites with a general formula ABO_3 (such as $BaTiO_3$, $SrTiO_3$, and $PbTiO_3$) have a cubic crystal structure in the paraelectric phase, with the small cation B in the center of an octahedron of oxygen ions and the large cations A at the corners of a cubic unit cell (Figure 1a). Barium titanate ($BaTiO_3$) has been particularly well studied in both single-crystal and ceramic forms.[6,7] Because of its high dielectric constant and ferroelectric properties, it has found applications in multilayer capacitors,[8] ferroelectric random access memory (FRAM),[9] temperature sensors,[10] electro-optic modulators,[11] and transducers and actuators.[2,12] Barium titanate can exist in four different phases depending on the temperature: the paraelectric cubic phase and ferroelectric tetragonal, orthorhombic, and rhombohedral phases. The cubic perovskite $BaTiO_3$ phase (space group $Pm\bar{3}m$) is stable above 120 °C. The

Received: September 29, 2011
Published: December 14, 2011

   dx.doi.org/10.1021/ja2091678 | J. Am. Chem.Soc. 2012, 134, 1136–1146

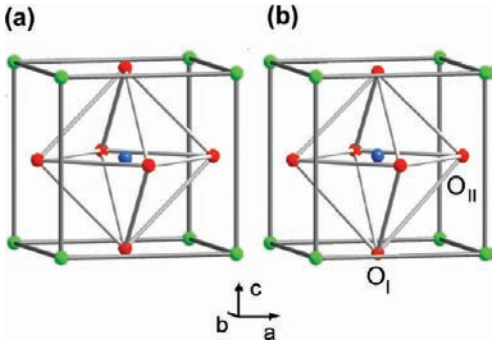

Figure 1. Unit cell structures of (a) cubic $BaTiO_3$ (space group $Pm\bar{3}m$) and (b) tetragonal $BaTiO_3$ (space group $P4mm$). Color code: Ba, green; O, red; Ti, blue. The positions of the asymmetric O atoms in the tetragonal phase are indicated as O_I and O_{II}.

lattice parameter a is 3.996 Å,[12,13] allowing enough room for the Ti^{4+} ion (radius of ca. 0.61 Å)[14] to move inside the $(O^{2-})_6$ cage. At temperatures between 120 and 0 °C, bulk $BaTiO_3$ adopts the tetragonal structure (space group $P4mm$), in which the Ti^{4+} ion moves off-center along a Ti−O bond (Figure 1b and Figure S1 in the Supporting Information). The resulting displacement gives a polarization of 26 $\mu C/cm^2$ along the ⟨001⟩ direction.[6,12,13] The original cubic symmetry is distorted by lengthening of the c lattice parameter (c/a ratio of 1.011).[12,13] If the origin is located at the O_{II} position, the displacements of the Ba^{2+}, Ti^{4+}, and O_I^{2-} ions along the c axis are +0.06, +0.12, and −0.03 Å, respectively.[15] Other phase transformations occur at lower temperatures and are practically less important for this study. Combined temperature-dependent investigations of the microscopic and macroscopic symmetry of $BaTiO_3$ have revealed that the phase transformation is a complex process involving both order−disorder and displacive mechanisms.[16−18]

A number of studies have indicated that the crystal lattice expands and the phase transition temperature decreases as the grain size is reduced. The ferroelectric phase can become unstable at room temperature when the particle size is reduced below a critical value.[19−21] Different critical sizes have been reported for perovskite lattices, ranging from over 100 nm[22,23] to a few unit cells.[24] The smallest nanocrystal size at which the tetragonal ferroelectric phase can be stabilized at room temperature is also strongly dependent on the surface structure, lattice defects, stress/strain, and dopant ions, making the phase transformation sensitive to the sample preparation method.[17,20,23,25]

One of the potentially viable approaches for imparting magnetic properties into ABO_3 lattices is to substitute B^{4+} with a transition-metal ion containing unpaired d electrons. The attempts to realize ferroelectric and ferromagnetic ordering simultaneously by replacing the B^{4+} cations in perovskite lattices with small transition-metal ions have generally led to reduced ferroelectricity.[2] This has been rationalized in terms of the importance of the hybridization between the d orbitals of the central cation and the 2p orbitals of oxygen for spontaneous ferroelectric phase stabilization. The d orbital occupancy, which is necessary for the formation of a net magnetic moment and for the long-range magnetic ordering, possibly hampers this hybridization process. In spite of the recent discovery of new multiferroic materials, understanding the coexistence of ferroelectricity and ferromagnetism and their interactions remains elusive. The synthesis of complex transparent conducting oxide (TCO) materials in the nanostructured form has been shown to be an effective way of controlling their phase, surface structure, and defects.[26] Controlling interfacial nanocrystal defects enables long-range magnetic ordering in transition-metal-doped TCOs prepared from analogous colloidal nanocrystals as building blocks.[27−29] The motivation of this work was to explore the possibility of introducing and controlling magnetic properties in doped nanostructured perovskite ferroelectrics and to understand the role of nanocrystal size, surface structure, and defects in mediating the magnetic ordering. Because $BaTiO_3$ has been a well-studied perovskite lattice, we used Cr^{3+}-doped $BaTiO_3$ nanocrystals (Cr^{3+}:$BaTiO_3$ NCs) as a model system for this study. Cr^{3+} is a kinetically stable ion with a high affinity for six-coordinate sites and no tendency to undergo Jahn−Teller distortion,[30] which could complicate the ferroelectric phase stabilization.[2] Although the incorporation of Cr^{3+} dopants suppresses the formation of the ferroelectric tetragonal phase, we observed the presence of the tetragonal phase at room temperature for NCs having an average size as small as ca. 7 nm and containing up to 5% substitutional dopant. Robust ferromagnetism was observed in ca. 0.5% Cr^{3+}:$BaTiO_3$ films prepared by spin-coating the substrates with suspensions of small-sized colloidal NCs. The long-range magnetic ordering in nanocrystalline films is associated with the formation of extended structural defects, which can mediate magnetic exchange interactions of the dopant ions, similarly to transition-metal-doped TCOs.[27−29] Magnetic circular dichroism (MCD) studies revealed that long-range Cr^{3+} ordering is the origin of the observed ferromagnetism. The saturation magnetization decreases with increasing doping concentration and NC size, likely because of increased antiferromagnetic interactions and a decreased interfacial defect concentration, respectively. This work allows for the preparation of colloidal perovskite NC building blocks having the optimal composition and size to achieve long-range magnetic ordering and retain the ferroelectric phase.

EXPERIMENTAL SECTION

Materials. Barium rods (99%), titanium(IV) isopropoxide [Ti{$OCH(CH_3)_2$}$_4$ or Ti(O-*i*-Pr)$_4$, 98%], chromium(III) acetylacetonate [$Cr(C_5H_7O_2)_3$ or $Cr(acac)_3$, 97.5%], chromium(III) chloride hexahydrate ($CrCl_3{\cdot}6H_2O$), and barium titanate powder ($BaTiO_3$, 99%) were all purchased from Strem Chemicals. Tri-*n*-octylphosphine oxide (TOPO, 90%) and benzyl alcohol ($C_6H_5CH_2OH$, 99%) were obtained from Sigma-Aldrich. Oleic acid, toluene, and ethanol were purchased from EMD Chemicals and used without further purification.

Synthesis of $BaTiO_3$ NCs. To prepare $BaTiO_3$ NCs from a few nanometers to several hundred nanometers in size, we used three different solvents in the solvothermal synthesis procedure: benzyl alcohol, ethanol, and water. $BaTiO_3$ NCs ca. 5 nm in size were synthesized in an inert atmosphere by modifying a previously reported procedure.[31] In a typical synthesis, 3 mmol of metallic Ba was dissolved in 20 mL of anhydrous benzyl alcohol at 80 °C until a slightly yellowish solution was obtained. The solution was cooled to room temperature, after which 1 molar equiv of Ti(O-*i*-Pr)$_4$ was added. The mixture was then stirred overnight, resulting in the formation of a gelled precipitate. This mixture was then transferred to a 45 mL Teflon liner of an acid digestion bomb (Parr) under an argon atmosphere and heated in an oven at 200 °C for 48 h.

For the synthesis of larger-sized NCs, a slightly different procedure was applied. The gelled suspension/precipitate mentioned above was centrifuged, and the supernatant was substituted with degassed ethanol or deionized water. After mixing the precipitate with the new solvent, the total volume was adjusted to be ca. 20 mL. Finally, this suspension was sealed in the Parr acid-digestion bomb and heated under the same conditions as described above.

dx.doi.org/10.1021/ja2091678 | J. Am. Chem.Soc. 2012, 134, 1136−1146

Synthesis and Surface Treatment of Cr^{3+}:$BaTiO_3$ NCs. Cr^{3+}:$BaTiO_3$ NCs were prepared using the same procedure described for the synthesis of pure $BaTiO_3$ NCs in different solvents, except that various amounts of $Cr(acac)_3$ were added to the reaction mixture along with metallic Ba. The starting molar ratio of $Cr(acac)_3$ to $Ti(O\text{-}i\text{-}Pr)_4$ was varied from 0.05 to 0.2. Considering a relatively low solubility of $Cr(acac)_3$ in water, a slightly altered methodology was also performed for water-synthesized samples to enhance the Cr^{3+} doping concentration: upon the formation of a gelled precipitate in the synthesis of pure $BaTiO_3$ NCs, different amounts of $CrCl_3{\cdot}6H_2O$ were dissolved in the water that was used to replace the benzyl alcohol supernatant.

After the digestion bomb was cooled to room temperature, the NCs were collected by centrifugation and washed three times with ethanol. To remove any surface-bound dopant ions and impurities, both pure and doped samples were suspended in melted TOPO, heated at 150 °C for 1 h, and then precipitated with ethanol.[32] This TOPO cleaning and precipitation procedure was repeated three times, yielding TOPO-capped Cr^{3+}:$BaTiO_3$ NCs. Benzyl alcohol- and ethanol-synthesized TOPO-capped NCs could be readily dispersed in toluene, but those prepared in water were less stable because of their larger size. To obtain colloidal suspensions of water-synthesized NCs, various dispersants such as polyelectrolytes, phosphate esters, and fatty acids were employed.[33] Among them, oleic acid proved to be the most effective. The surface-cleaned TOPO-capped NCs were heated in oleic acid at 100 °C for 30 min and then precipitated and washed with ethanol. Oleic acid-capped NCs were suspended relatively well in hexane or toluene.

Characterization and Measurements. Powder X-ray diffraction (XRD) patterns were collected using an INEL diffractometer with a position-sensitive detector, and monochromatic Cu Kα radiation. The morphology and structure of the NCs were studied by scanning electron microscopy (SEM) with a LEO FESEM 1530 microscope operating at 5 kV and by transmission electron microscopy (TEM) with a JEOL-2010F microscope operating at 200 kV. Gatan DigitalMicrograph software was used to analyze the TEM images. The doping concentrations were determined by inductively coupled plasma atomic emission spectroscopy (ICP-AES) and X-ray photoelectron spectroscopy (XPS) and are expressed as a percentage of substituted Ti^{4+} ions. Raman spectra were recorded at room temperature with a Renishaw 1000 spectrometer using a He−Ne laser with the excitation wavelength of 632.8 nm. The measurements were performed at ca. 10% of the maximum laser output power (40 mW). The spectrometer was calibrated using a silicon standard. The optical absorption spectra of colloidal NCs were collected in standard 1 cm path length quartz cuvettes with a Varian Cary 5000 spectrophotometer. For low-temperature absorption and MCD measurements, the colloidal suspensions were deposited on high-quality quartz disks and mounted in the appropriate cryostats. Low-temperature absorption spectra were measured using a liquid helium optical cryostat (Optistat CF, Oxford). MCD measurements were performed with a Jasco J-815 spectropolarimeter using a high-field superconducting magneto-optical cryostat (SM4000-8, Oxford) with a variable-temperature (1.5−300 K) and variable-magnetic-field (0−8 T) compartment positioned in the Faraday configuration. The magnetization was measured with a Physical Property Measurement System (PPMS, Quantum Design) in ACMS mode. For measurements of free-standing NCs, the NC powders were precipitated with ethanol, air-dried, and loaded as powders into measurement capsules. For measurements of nanocrystalline films, the colloidal NCs were spin-coated multiple times on clean, accurately weighed sapphire substrates with mild annealing at 300 °C for 1 min between consecutive coatings. The final nanocrystalline films were weighed again on an analytical balance to determine the magnetization per unit mass of the samples. All samples were handled identically under carefully controlled magnetic-contamination-free conditions. X-ray MCD (XMCD) measurements were performed in scanning transmission X-ray microscopy (STXM) configuration at the SM beamline (10ID-1) of the Canadian Light Source (CLS). For XMCD measurements, a ferromagnetic sample was transferred from the nanocrystalline film to a sample holder window by dry pressing. The sample holder was mounted on a magnetic ring (ca. 0.1 T), allowing for a parallel orientation of the magnetic field and X-ray beam propagation directions. Image stacks were collected at ca. 300 K by imaging a selected area of the sample with different energies at the Cr $L_{2,3}$ edge from 565.0 to 595.0 eV using both left-circularly polarized (LCP, ρ^-) and right-circularly polarized (RCP, ρ^+) photons. The analysis of the images and spectra was performed using Axis 2000 software after the images were aligned using Jacobson Analysis software. The aligned image stack containing the information about the transmitted intensities for each photon energy and helicity was then converted into optical density (OD) values using the relation $\ln(I/I_0)$, where I is the signal transmitted through a desired sample area and I_0 is the signal from the image area without the sample. The Cr $L_{2,3}$-edge XMCD spectrum was derived as the difference in absorbance between left- and right-circularly polarized X-rays.

RESULTS AND DISCUSSION

Synthesis and Size Control of $BaTiO_3$ NCs. The proposed reaction mechanism for the synthesis method applied in this work involves the formation of a C−C bond between the isopropoxy ligand of $Ti(O\text{-}i\text{-}Pr)_4$ and benzyl alcohol, accompanied by the release of the hydroxyl group from benzyl alcohol.[31] The Ti−OH group generated in the process undergoes further condensation along with the formation of 4-phenyl-2-butanol. Dissolving barium in benzyl alcohol before the addition of the metal alkoxide allows for the generation of benzyl alcoholate as a plausible base activator of the nucleophilic attack of a β-carbon atom of the isopropoxide on the benzylic carbon atom and also for the formation of the Ba−O−Ti bond.[31] The obtained bimetallic alkoxide precursor containing both Ba and Ti decomposes during the heating procedure, resulting in $BaTiO_3$ NCs.[31,34] In the solvothermal preparation of $BaTiO_3$ NCs, the choice of the solvent is critical for the determination of the NC size.[21,35−38]

Figure 2 shows electron microscopy images of $BaTiO_3$ NCs prepared in (a) water, (b) ethanol, and (c) benzyl alcohol. The nanocrystals synthesized in water have a quasi-spherical shape and sizes of 100−200 nm (Figure 2a and Figure S2), with a number-average diameter of 166 ± 65 nm. The NCs prepared in ethanol (Figure 2b) and benzyl alcohol (Figure 2c) have a sheetlike morphology (thin-layered nanostructures) with average sizes of 6.7 ± 1.7 and 4.6 ± 1.3 nm, respectively. The NC sizes of these samples were consistently measured for the longest particle dimension, and the average size was determined as an ordinary arithmetic mean (number average). The size of NCs prepared in different solvents is determined by the rate of NC nucleation and growth.[21] Generally speaking, small NCs tend to dissolve rather quickly, and the solvated ions are more stable in polar solvents than in nonpolar ones. In nonpolar solvents with a low dielectric constant, the saturation of ions in solution is reached rapidly, accelerating the nucleation rate and leading to the stabilization of small NCs.[36] In contrast, the high solubility of ions in high-dielectric-constant solvents leads to the formation of fewer nuclei in the initial stage of the NC growth, resulting in the formation of larger NCs. The room-temperature dielectric constants of the three solvents used in this work are 80.1 (water), 24.3 (ethanol), and 13.0 (benzyl alcohol). As expected, the sample preparation in water produced larger NCs in comparison to that in ethanol or benzyl alcohol. Moreover, the employed solvents also acted as capping ligands by adsorbing to NC surfaces, thus limiting their growth.[37] The bulky molecules on the NC surfaces could prevent further reaction, suppressing

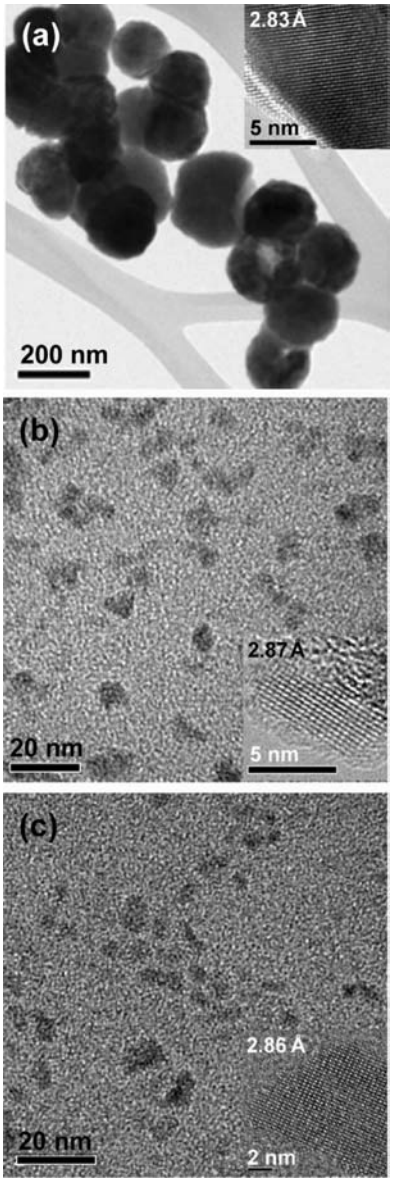

Figure 2. TEM images of $BaTiO_3$ NCs synthesized in (a) water, (b) ethanol, and (c) benzyl alcohol. Insets: lattice-resolved images of typical NCs showing measured *d* spacings.

the NC attachment and growth. The geometry of the solvent molecules could therefore also be an important factor in controlling the NC size. The effect of steric hindrance decreases in the order phenylmethanolate > ethanolate > hydroxide. Accordingly, capping NCs with phenylmethanolate or ethanolate could effectively passivate the NC surfaces, leading to the formation of smaller NCs relative to those synthesized in water. Lattice-resolved TEM images of isolated NCs (shown in the corresponding insets in Figure 2) indicate that nanoparticles in all three samples are single-crystalline. The measured *d* spacings range from 2.83 to 2.87 Å. Because the crystal structures of cubic and tetragonal $BaTiO_3$ are closely related, the *d* spacing of the two phases is very similar. The *d* spacing of the (110) plane is 2.85 Å for the cubic phase and 2.825 Å for the tetragonal phase. Although the measured *d* spacings would indicate mostly tetragonal phase for NCs prepared in water and mostly cubic phase for those prepared in ethanol and benzyl alcohol, given the uncertainly in these measurements it is difficult to assign the *d* spacings unambiguously to either of these two phases. Similarly, Kolen'ko et al.[35] performed selected-area electron diffraction (SAED) measurements to identify the structure of $BaTiO_3$ nanoparticles, but the weakly resolved rings did not allow for conclusive identification. Therefore, further characterization is needed for the crystal structure determination.

In comparison with the synthesis of NCs in the presence of surfactants, the solvent-controlled methods offer several other advantages important for this study, including high purity of the product and reduced toxicity. Furthermore, the synthesis temperature is significantly lower than typical temperatures applied in traditional solid-state methodologies, which decreases the likelihood of secondary phase formation, especially when a dopant is introduced into the reaction mixture. This low-temperature solvent-controlled synthesis offers a promising cost-effective approach for producing doped $BaTiO_3$ NCs with high purity and adjustable size.

Structure and Phase Transformation of $BaTiO_3$ NCs. XRD patterns of typical $BaTiO_3$ NC samples synthesized in water, ethanol, and benzyl alcohol are shown in Figure 3a.

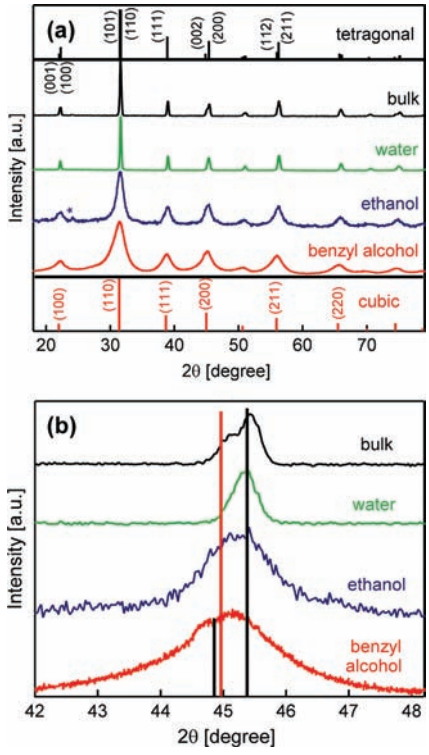

Figure 3. (a) XRD patterns of $BaTiO_3$ NCs synthesized in different solvents, as indicated in the graph. Vertical red (bottom) and black (top) lines represent the XRD patterns of bulk cubic (JCPDS no. 31-0174) and tetragonal (JCPDS no. 05-0626) $BaTiO_3$, respectively. (b) Narrow-range, high-resolution XRD patterns of the same samples indicating the position of the cubic-phase (200) reflection (red line) and tetragonal-phase (200) and (002) reflections (black lines).

Commercial bulk powder was also studied for comparison. The XRD patterns of all samples are consistent with the cubic or tetragonal $BaTiO_3$ structure. Only a small amount of $BaCO_3$ byproduct was detected in the ethanol-synthesized sample (marked with asterisk); $BaCO_3$ is a very common impurity in the synthesis of $BaTiO_3$ and can usually be removed by washing with an acid.[35] From the Debye–Scherrer analysis of the (100),

dx.doi.org/10.1021/ja2091678 | J. Am. Chem.Soc. 2012, 134, 1136–1146

(110), and (111) diffraction peaks, the average grain sizes were estimated to be 4 and 7.5 nm for the benzyl alcohol- and ethanol-synthesized NCs, respectively, in good agreement with the average NC sizes determined from the TEM images. The instrumental line width, however, limited the determination of the sizes of NCs synthesized in water. The 2θ range between 40° and 50° is commonly used to distinguish the cubic and tetragonal phases, where the single (200) peak characteristic of the cubic structure splits into the two tetragonal peaks, (200) and (002).[39] However, it is still difficult to assign the crystal structure of small NCs using conventional X-ray diffractometers because of the significant line broadening caused by a short coherence length. Despite these difficulties, closer inspection of this range still reveals some interesting findings. Bulk $BaTiO_3$ powder exhibits an apparent splitting of the (200) peak, as expected for the tetragonal phase at room temperature (Figure 3b, black trace). The splitting is less distinct for NCs prepared in this work, indicating a gradual change of the average NC structure from tetragonal to cubic as the grain size decreases at the nanoscale. For water-synthesized NCs, the peak position still matches the tetragonal (200) reflection. This peak also has an asymmetric shape, indicating the existence of another feature at lower 2θ values caused by either the tetragonal structure itself [i.e., the (002) peak] or the coexistence of tetragonal and cubic phases. This tetragonal structure might partly be a consequence of averaging ⟨111⟩ displacements of octahedral Ti^{4+} (local rhomboherdal structure),[40] although these distortions cannot be conclusively identified from the present results. The presence of the cubic phase becomes more apparent for NCs synthesized in ethanol and benzyl alcohol, for which the peak shift to lower 2θ values is evident, despite significant broadening. Importantly, even for NCs synthesized in benzyl alcohol, this XRD feature still shows a manifest asymmetry and splitting, suggesting some contribution of the tetragonal phase for NCs having an average size of ca. 4.6 nm. The observed shift of the tetragonal (200) peak to lower angles in benzyl alcohol-synthesized NCs might also be partly associated with the crystal lattice expansion. An increase in the unit cell volume with decreasing grain size has been shown for several metal oxides.[21,41,42] Tsunekawa et al.[43] demonstrated that the lattice constant a increases anomalously in both tetragonal and cubic $BaTiO_3$ nanoparticles as a result of changes in the bonding character of Ti^{4+} ions. The elongation of the lattice constant a was determined to be greater than 2.5% in 15 nm NCs.[43] A possible explanation of this phenomenon is that the competition between the long-range Coulombic attractive interactions and the short-range repulsive interactions in ionic NCs creates an effective negative pressure, leading to a volume expansion in small oxide particles.[44]

In addition to XRD analysis, which gives an average and static symmetry, the local and dynamic symmetry of hydrothermally and solvothermally produced $BaTiO_3$ NCs was monitored by Raman spectroscopy.[16,45] Raman scattering is a highly sensitive spectroscopic probe of the local structure of atoms and can be used to analyze the structure of $BaTiO_3$ samples. According to the selection rules, $BaTiO_3$ with ideal cubic symmetry should be Raman-inactive.[21,39,46] In the cubic-phase O_h symmetry, the four optical modes transform as one T_{2u} and three T_{1u} irreducible representations. The T_{2u} mode is silent, and the threefold-degenerate T_{1u} modes are only IR-active. High-temperature Raman spectra, however, still show the existence of two broad bands at ca. 260 and 530 cm^{-1}, which has been attributed to the local Ti^{4+} ion disorder.[16,46] For the tetragonal C_{4v} point-group symmetry, T_{1u} and T_{2u} split into A_1, E, and B_1 modes. Long-range electrostatic forces induce the splitting of the A_1 and E modes into transverse (TO) and longitudinal (LO) phonons, giving a total of 10 Raman-active modes.

Figure 4 shows Raman spectra of commercial $BaTiO_3$ powder and the NC samples prepared in water, ethanol, and

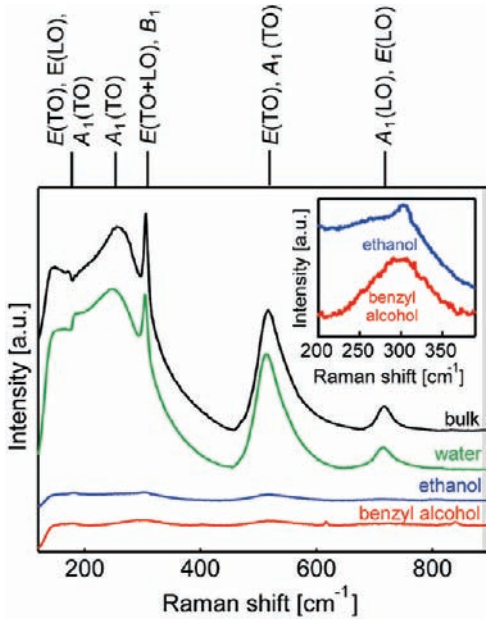

Figure 4. Raman spectra of $BaTiO_3$ NCs prepared in different solvents, as indicated in the graph. The assignments of the Raman modes are indicated at the top of the graph. Inset: enlarged spectrum in the E(TO + LO), B_1 region (ca. 306 cm^{-1}) for NCs synthesized in ethanol (blue) and benzyl alcohol (red).

benzyl alcohol. The assignments of the tetragonal $BaTiO_3$ peaks (shown in the graph) are based on those previously reported in the literature.[21,39,47] All of the spectra exhibit broad features associated with disorder of the Ti^{4+} ions within individual unit cells. As evident from Figure 4, the Raman spectrum of a commercial $BaTiO_3$ powder is in excellent agreement with that expected for the tetragonal phase. It is widely accepted that the tetragonal-to-cubic phase transition can be identified by the disappearance of the E(TO + LO), B_1 peak at ca. 306 cm^{-1} and the A_1(LO), E(LO) peak at ca. 717 cm^{-1}, which are specific to the tetragonal phase.[16,48] For NCs prepared in different solvents, all phonon modes become weaker and broader. The water-synthesized NCs reveal only minor weakening and broadening of the characteristic peaks centered at 306 and 717 cm^{-1}, a clear evidence of a high degree of tetragonality in 100−200 nm NCs. The intensities of these two bands decrease rapidly for the NCs synthesized in ethanol and benzyl alcohol, which are smaller than 10 nm, but their frequencies remain essentially unchanged. Although the spectra of ethanol- and benzyl alcohol-synthesized $BaTiO_3$ NCs appear similar, careful inspection of the 200−350 cm^{-1} range (Figure 4 inset) shows a notable difference. A distinct peak at ca. 306 cm^{-1}, which is observed for ethanol-synthesized NCs, is absent for NCs synthesized in benzyl alcohol. This feature, along with a broad peak centered at ca. 717 cm^{-1}, indicates the presence of the tetragonal crystal structure in ca. 6.7 nm NCs synthesized in ethanol, at least as microscopic domains in pseudocubic

dx.doi.org/10.1021/ja2091678 | J. Am. Chem.Soc. 2012, 134, 1136−1146

$BaTiO_3$ NCs. The increased line width of this transition indicates a structural decoherence, or a lower extent to which this tetragonality expands by long-range ordering. Taken together, the XRD and Raman spectroscopy results indicate some retention of the extended tetragonal structure in ethanol-synthesized $BaTiO_3$ NCs. While the signature of average tetragonality has been observed for NCs ranging from 20 to 30 nm in size,[21,39,45,49] our observation pushes this size limit to ca. 7 nm. Although a sharp feature at 306 cm^{-1} completely vanishes for the smallest NCs prepared in benzyl alcohol, it is worth noting that Raman scattering peaks can still be observed at ca. 297, 520, and 720 cm^{-1}, which is not expected for ideal cubic symmetry. Shiratori et al.[39] attributed this to a mixture of the dominant cubic phase and traces of local tetragonality. Similarly, recent neutron scattering measurements have also revealed a strong local tetragonal distortion (off-centering of the central Ti^{4+} ion) in metrically cubic ca. 5 nm diameter $BaTiO_3$ NCs.[40] It is therefore likely that NCs prepared in benzyl alcohol have a cubic crystal structure with tetragonal distortions at the local or unit cell level. Another interesting observation associated with the properties of $BaTiO_3$ is a spectral feature at ca. 180 cm^{-1} that is transformed from a spectral dip for the bulk powder to a peak for the NC samples. It has been suggested that this dip is characteristic of depolarized single crystals and polycrystalline samples and results from anharmonic coupling among the three A_1(TO) phonons.[39,47] The positive peak in the same spectral range has been observed for nanocrystalline powders prepared by hydrothermal and sol–gel methods[12] and is related to damping of A_1(TO) modes caused by lattice defects or internal pressure in nanometer-sized grains.[39]

Effect of the Cr^{3+} Dopant on the $BaTiO_3$ NC Structure. Cr^{3+} dopants in the $BaTiO_3$ lattice preferentially substitute for Ti^{4+} ions because of the similarity of their ionic radii in octahedral coordination [$r(Cr^{3+})$ = 0.62 Å, $r(Ti^{4+})$ = 0.61 Å], creating in the process oxygen vacancies to allow for charge compensation.[50] XRD patterns of Cr^{3+}:$BaTiO_3$ NCs prepared in water and having different Cr^{3+} doping concentrations are compared with XRD patterns of undoped NCs and bulk powder in Figure 5a. Similarly to undoped NCs, the long-averaged XRD patterns of the Cr^{3+}-doped samples reveal highly crystalline $BaTiO_3$ without any byproducts or secondary phases, even at high doping concentrations. The sizes of doped $BaTiO_3$ NCs remain similar to those of undoped NCs, as evidenced from the unchanged XRD peak broadening. The peaks, however, experience a gradual shift to lower 2θ values with increasing doping concentration.

The influence of Cr^{3+} incorporation on the structure of $BaTiO_3$ NCs can be studied by examining the (200) XRD region (2θ = 44–46.5°), similarly to undoped NCs (Figure 5b). With increasing doping concentration, the tetragonal (200) and (002) peaks merge into a single peak, suggesting the tetragonal-to-cubic phase transformation. The XRD pattern of the most highly doped NCs (ca. 10.5%) indicates the dominant cubic phase. Similar results were obtained for Cr^{3+}:$BaTiO_3$ NCs synthesized in other solvents, although traces of $BaCO_3$ impurity were occasionally observed as the NCs decreased in size (Figure S3). Typical (200) XRD patterns of Cr^{3+}:$BaTiO_3$ NCs synthesized in ethanol and benzyl alcohol are shown in Figure 5c,d, respectively. The peak shift to lower angles along with its narrowing and a decrease in asymmetry are suggestive of a transformation from the tetragonal phase to the cubic phase with increasing doping concentration (black to red traces). These changes are more subtle than in the case of water-synthesized NCs because of the smaller grain sizes (more extensive XRD broadening).

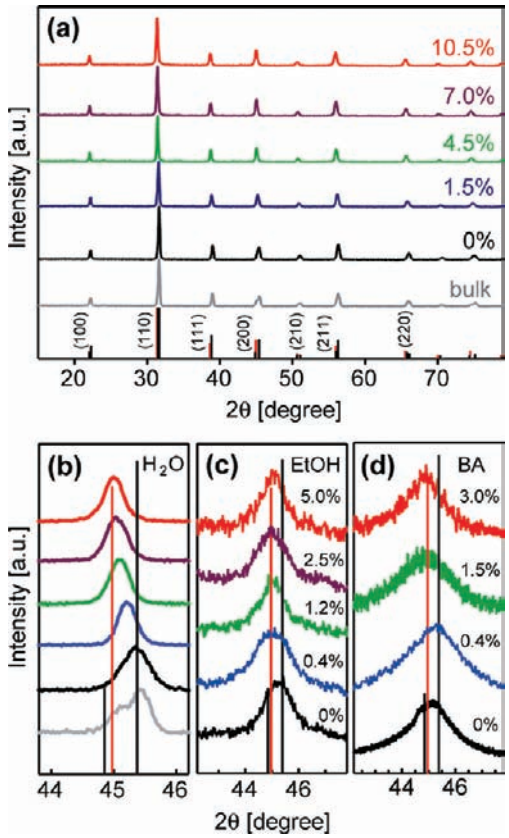

Figure 5. (a) Overview XRD patterns of water-synthesized Cr^{3+}:$BaTiO_3$ NCs having different doping concentrations, as indicated in the graph. Vertical red and black lines represent the XRD patterns of bulk cubic (JCPDS no. 31-0174) and tetragonal (JCPDS no. 05-0626) $BaTiO_3$, respectively. (b–d) Narrow-range, high-resolution XRD patterns of Cr^{3+}:$BaTiO_3$ NCs synthesized in (b) water, (c) ethanol, and (d) benzyl alcohol indicating the positions of the cubic-phase (200) reflection (red line) and tetragonal-phase (200) and (002) reflections (black lines). The doping concentrations corresponding to the XRD patterns are indicated in the graphs. The doping concentrations in (b) are the same as those in (a).

The interplay between NC tetragonality, size, and doping concentration of Cr^{3+}:$BaTiO_3$ NCs was further investigated by Raman spectroscopy. Figure 6 shows Raman spectra of Cr^{3+}:$BaTiO_3$ NCs synthesized in water. Consistent with the XRD results, the tetragonal structure is gradually suppressed with increasing doping concentration, as judged by the reduced peak intensities and enhanced peak broadenings. Importantly, the tetragonal phase is locally retained even in highly doped NCs, as evidenced by the presence of a peak at 305 cm^{-1} (Figure 6 inset) assigned to the E(LO + TO), B_1 mode. Comparison with the XRD results, which are consistent with predominantly cubic structure (Figure 5b), indicates that the phase transition in doped NCs is also a complex interplay between order–disorder and displacive mechanisms.

As expected, the tetragonality and phase coherence also decreased in ethanol- and benzyl alcohol-synthesized Cr^{3+}:$BaTiO_3$ NCs. Figure 7a shows Raman spectra of ethanol-synthesized Cr^{3+}:$BaTiO_3$ NCs with different doping concentrations. The peak intensities gradually decrease, although even at doping concentration of ca. 5% the

dx.doi.org/10.1021/ja2091678 | J. Am. Chem.Soc. 2012, 134, 1136–1146

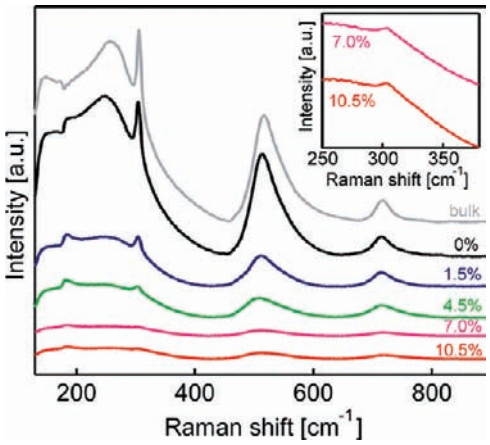

Figure 6. Raman spectra of water-synthesized Cr^{3+}:$BaTiO_3$ NCs having different doping concentrations, as indicated in the graph. Inset: enlarged spectra in the E(TO + LO), B_1 region (ca. 306 cm^{-1}) for high Cr^{3+} dopant concentrations.

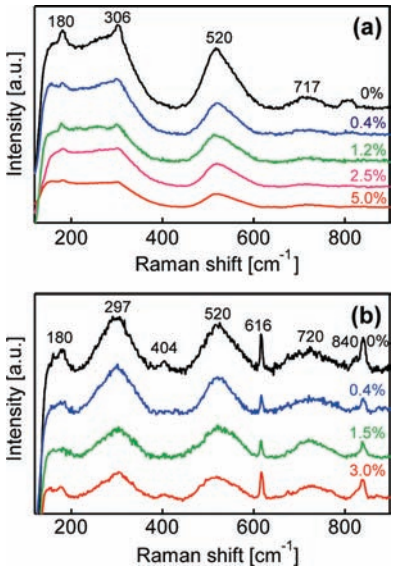

Figure 7. Raman spectra of Cr^{3+}-doped $BaTiO_3$ NCs synthesized in (a) ethanol and (b) benzyl alcohol and having different doping concentrations, as shown in the graph. The positions of the maxima of the observed peaks are indicated in the graphs.

characteristic peak at 305 cm^{-1} can still be clearly observed, confirming the coexistence of the ferroelectric phase. The Raman spectra of Cr^{3+}:$BaTiO_3$ NCs synthesized in benzyl alcohol show much less pronounced tetragonal peaks (Figure 7b). The band shapes and intensities of these spectra are consistent with highly localized displacement of Ti^{4+} ions in the cubic lattice. It is also evident that the formation of additional non-chromium-based impurity modes becomes more likely with decreasing NC size. The peak at 800−850 cm^{-1} is an indication of hydroxyl defects.[17,39] The 404 and 616 cm^{-1} modes may arise from $BaCO_3$, anatase TiO_2, or rhombohedral $BaTiO_3$.[51] Direct comparison of the two effects that control phase stabilization in doped $BaTiO_3$ NCs at room temperature—size and doping concentration—is critical for the rational design of multiferroic nanostructures. Among all of the prepared samples, pure $BaTiO_3$ NCs prepared in water exhibit the highest tetragonality. The comparison between undoped ethanol-synthesized $BaTiO_3$ NCs and 10.5% Cr^{3+}:$BaTiO_3$ NCs synthesized in water reveals that ca. 6.7 nm undoped NCs prepared in ethanol are significantly more tetragonal despite being an order of magnitude smaller in size (Figure S4). This comparison implies that the doping concentration has a dominant effect on the phase stabilization and suggests that a possible approach for introducing long-range magnetic ordering in ferroelectric tetragonal-phase $BaTiO_3$ NCs should rely on using NCs with as low a doping concentration as necessary to support ferromagnetic exchange interactions.

Ligand-Field Electronic Absorption Spectroscopy of Cr^{3+}:$BaTiO_3$ NCs. The electronic absorption spectroscopy of six-coordinate Cr^{3+} ion has been extensively studied in the past and played a historically important place in the development of ligand-field theory.[30] A typical electronic absorption spectrum of colloidal TOPO-treated Cr^{3+}:$BaTiO_3$ NCs synthesized in benzyl alcohol are shown in Figure S5. Two characteristic ligand-field bands at ca. 15 850 and ca. 23 200 cm^{-1} can be identified and assigned to $^4A_2 \rightarrow {}^4T_2(F)$ and $^4A_2 \rightarrow {}^4T_1(F)$ d−d transitions, respectively, of pseudo-octahedral Cr^{3+}. The $^4A_2 \rightarrow {}^4T_1(F)$ transition is only weakly observed as a broad shoulder because of tailing of the solvent (toluene) and possibly charge transfer absorption into the visible region. To demonstrate internal Cr^{3+} doping of $BaTiO_3$ NCs, we compared the ligand-field absorption spectra after one and three TOPO treatments (Figure S6).[32] A subtle shift of the $^4A_2 \rightarrow {}^4T_2(F)$ transition upon TOPO treatment is associated with a removal of the surface-bound dopant ions. Additional TOPO treatments do not lead to the spectral change, indicating quantitative removal of the surface-bound dopant ions. Similar observations have been reported for Cr^{3+}-doped SnO_2 and In_2O_3 NCs.[28,29,32]

Investigation of the Cr^{3+} ligand-field transitions can also provide deeper understanding of the phase stabilization of doped $BaTiO_3$ NCs with respect to the NC size and doping concentration. The $^4A_2 \rightarrow {}^4T_2(F)$ absorption band for ethanol- and benzyl alcohol-synthesized NCs with different doping concentrations are displayed in Figure 8a,b, respectively.[52] For both solvents, the peak center of gravity shifts to lower energy with increasing doping concentration. This d−d absorption transition is sensitive to the ligand-field strength of the Cr−O bonds and therefore should depend on the lattice symmetry. The observed shifts are consistent with a decrease in the ligand-field strength as the tetragonality is diminished with increasing doping concentration. It has been shown that the decline in tetragonality due to decreasing NC size is accompanied by expansion of the unit cell volume in $BaTiO_3$.[21,42] Although experimental results on the interionic distances in doped $BaTiO_3$ NCs are lacking in the literature, previous reports have demonstrated that the Ti−O, Ba−O, and Ba−Ti distances in pure $BaTiO_3$ increase with decreasing particle size and increasing electrostatic repulsion.[43] Our spectroscopic results suggest that the unit cell volume and the average Cr−O distance also increase with increasing doping concentration because of the loss of tetragonality.

The size contribution to the ligand-field strength in doped $BaTiO_3$ NCs can be inferred by considering the ligand-field spectra of ethanol- and benzyl alcohol-synthesized NCs having similar doping concentrations. The spectra of Cr^{3+}:$BaTiO_3$ NCs prepared in ethanol (2.5% Cr^{3+}) and benzyl alcohol (3.0% Cr^{3+}) are shown in Figure 8c. A red shift of ca. 700 cm^{-1} for the benzyl alcohol-synthesized sample relative to the ethanol-synthesized one suggests a significant structural change

dx.doi.org/10.1021/ja2091678 | J. Am. Chem.Soc. 2012, 134, 1136−1146

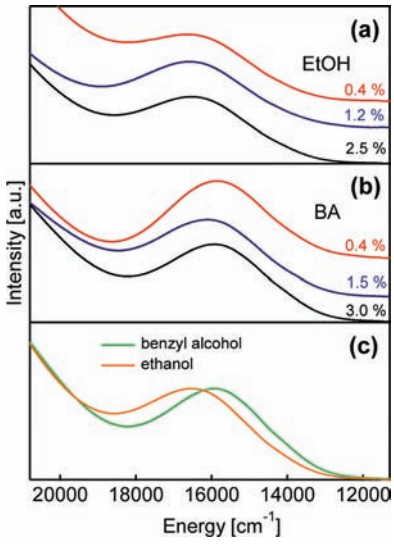

Figure 8. (a, b) Cr^{3+} [$^4A_2 \rightarrow {}^4T_2(F)$] 300 K ligand-field spectra of Cr^{3+}:$BaTiO_3$ NCs synthesized in (a) ethanol and (b) benzyl alcohol and having different doping concentrations, as indicated in the graphs. (c) Comparison of the Cr^{3+} [$^4A_2 \rightarrow {}^4T_2(F)$] spectrum for 2.5% Cr^{3+}:$BaTiO_3$ NCs prepared in ethanol (orange trace) and 3.0% Cr^{3+}:$BaTiO_3$ NCs prepared in benzyl alcohol (green trace).

in the crystal lattice. As concluded previously, 4.6 nm NCs synthesized in benzyl alcohol possess a larger degree of cubic symmetry and a larger unit cell volume than those synthesized in ethanol. These data demonstrate the possibility of tuning the electronic structure and interactions of transition-metal dopants in $BaTiO_3$ NCs by adjusting the doping concentration and NC size via changes in the synthesis conditions.

Magnetic and Magneto-optical Properties of Cr^{3+}:$BaTiO_3$ NCs. Figure 9b shows 4.5 K MCD spectra of colloidal 0.4% Cr^{3+}:$BaTiO_3$ NCs prepared in ethanol. The spectra were collected in a variable magnetic field of 1−7 T. Figure 9a presents a typical 300 K absorption spectrum. A broad $^4A_2 \rightarrow {}^4T_2(F)$ transition in the absorption spectrum centered at 16 500 cm^{-1} shows well-resolved MCD structure. In particular, a relatively narrow asymmetric and structured feature at ca. 14 400 cm^{-1} overlaps with the $^4A_2 \rightarrow {}^4T_2(F)$ transition on the low-energy side. This peak can be readily assigned to the formally spin-forbidden $^4A_{2g} \rightarrow {}^2E$, $^2T_2$ transitions. Pronounced intensity of these doublets in MCD spectra indicates a high sensitivity of MCD to transition-metal-based transitions.[53] Furthermore, the intensity and splitting of all Cr^{3+} transitions are significantly more pronounced for ethanol-synthesized than for benzyl alcohol-synthesized Cr^{3+}:$BaTiO_3$ NCs having cubic crystal structure (Figure S7), which is consistent with relaxation of the Laporte selection rule due to the reduction of Cr^{3+} symmetry in tetragonal $BaTiO_3$. A barely observed $^4A_2 \rightarrow {}^4T_1(F)$ shoulder in the absorption spectrum appears as a strong negative transition centered at 24 200 cm^{-1}. It is likely that this transition is mixed with a charge-transfer transition involving the NC host lattice, on the basis of the tailing absorption spectrum and magnetization dependence (see below). In addition to elucidating the electronic structure of Cr^{3+} dopant ions, MCD allows for molecular-level detection of the magnetization properties. The Figure 9b inset shows a plot of the monochromatic intensities of Cr^{3+} transitions as a function of the applied magnetic field. With the g value of 1.975 for Cr^{3+} in $BaTiO_3$,[54] the intensities at 14 390, 16 585, and 20

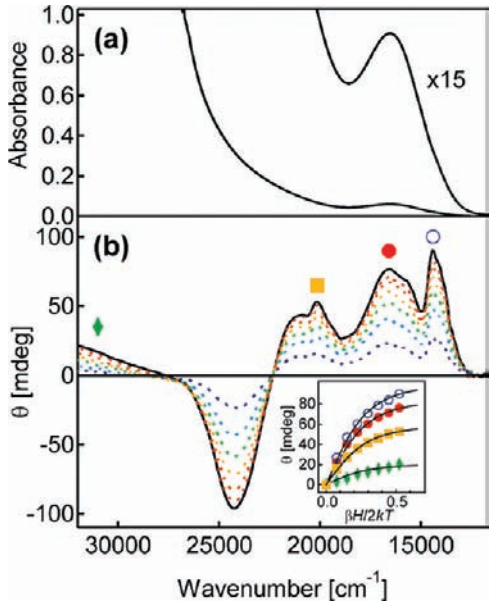

Figure 9. (a) Electronic absorption spectrum at 300 K of 0.4% Cr^{3+}:$BaTiO_3$ NCs synthesized in ethanol. The same spectrum is shown multiplied by a factor of 15 for clarity. An essentially identical spectrum was obtained at 5 K. (b) MCD spectra at 4.5 K of the same Cr^{3+}:$BaTiO_3$ NCs collected at magnetic fields of 1−7 T in increments of 1 T. Inset: MCD intensities at different spectral positions plotted as a function of the applied magnetic field. The spectral positions are labeled with the corresponding symbols in the graph. The black lines are fits to the Brillouin function (eq 1), as described in the text.

120 cm^{-1} were well-fit to the spin-only Brillouin function for the spin state $S = {}^3/_2$ (eq 1):

$$M_S = \frac{1}{2} N g \mu_B \left\{ (2S+1) \coth\left[(2S+1)\left(\frac{g\mu_B H}{2k_B T} \right) \right] - \coth\left(\frac{g\mu_B H}{2k_B T} \right) \right\} \quad (1)$$

where N, μ_B, and k are the total number of dopants per unit volume, the Bohr magneton, and the Boltzmann constant, respectively; T is the temperature; and H is the magnitude of the magnetic field. A close fit to the spin-only Brillouin function suggests the presence of isolated paramagnetic Cr^{3+} ions in $BaTiO_3$ NCs. The fit to the Brillouin function slightly deviates for higher-energy spectral positions (i.e., 31 000 cm^{-1} in Figure 9), indicating the contributions from the charge-transfer transitions involving the $BaTiO_3$ NC host lattice. Typical magnetic susceptibility data for free-standing ethanol-synthesized 0.4% Cr^{3+}:$BaTiO_3$ NCs were also readily fit to the Brillouin expression (Figure S8), supporting the conclusion that Cr^{3+} ions exist as isolated paramagnetic species within the NCs.

Motivated by the successes in using paramagnetic transition-metal-doped transparent conducting oxide (TCO) NCs for the preparation of transparent magnetic semiconductor films,[27−29] we applied the same approach in this study. This method could enable the use of doped ferroelectric NCs as building blocks for multiferroic materials. The long-range ordering in nanocrystalline transition-metal-doped TCO films prepared from colloidal NCs has been associated with the existence of extended structural (grain boundary) defects at the NC interfaces, which

dx.doi.org/10.1021/ja2091678 | J. Am. Chem.Soc. 2012, 134, 1136−1146

have a role in mediating the magnetic ordering of dopant ions.[29,55,56] The networking of NCs in these films also causes an increase in the size of the magnetic domains that helps stabilize the ferromagnetic phase. This phenomenon has been observed for different dopants in different TCO NCs, suggesting the generality of this interfacial defect-induced dilute magnetic ordering mechanism.[27,28,32,55] Since $BaTiO_3$ is also a complex oxide material that should exhibit surface chemistry similar to that of TCOs, it is reasonable to expect that defect formation in Cr^{3+}:$BaTiO_3$ NC films may also result in long-range magnetic ordering by the same defect-related mechanism. Figure 10 shows 300 K magnetic hysteresis loops

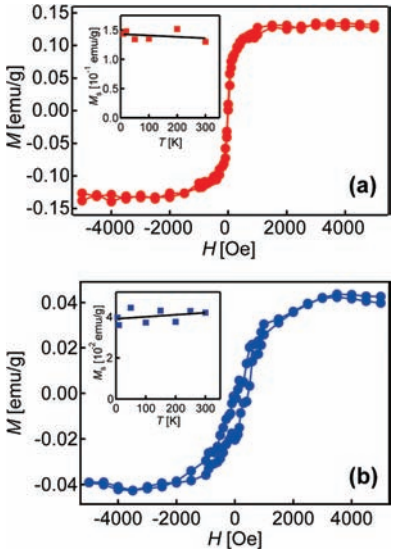

Figure 10. Magnetization data at 300 K for Cr^{3+}:$BaTiO_3$ nanocrystalline films prepared from (a) 0.4% Cr^{3+}-doped NCs synthesized in benzyl alcohol and (b) 0.4% Cr^{3+}-doped NCs synthesized ethanol. Insets: Saturation magnetization as a function of temperature. Black lines are linear fits indicating the absence of a magnetic phase transition below room temperature.

of nanocrystalline films prepared from 0.4% Cr^{3+}:$BaTiO_3$ NCs synthesized in benzyl alcohol (Figure 10a) and ethanol (Figure 10b). The hysteresis loops show robust ferromagnetic behavior, with saturation magnetic moments of 1.95 and 0.53 μ_B/Cr^{3+}, respectively. The temperature dependence of the saturation magnetization (Figure 10 insets) confirms that the magnetic phase transition temperature (T_C) for both samples is above room temperature. Control experiments on $BaTiO_3$ films prepared in the identical way from undoped NCs revealed only diamagnetic interactions. Similarly, the magnetization data for free-standing Cr^{3+}:$BaTiO_3$ NCs confirmed their paramagnetic nature (Figure S9).

For the development of the rational approach to fabrication of nanostructured multiferroic materials, it is instructive to compare the magnetization properties of the two films studied in Figure 10. The saturation magnetization of benzyl alcohol-synthesized Cr^{3+}:$BaTiO_3$ NCs is significantly larger than that of NCs synthesized in ethanol. This observation can be explained by the larger surface-to-volume ratio of nanocrystalline films fabricated from the smaller NCs synthesized in benzyl alcohol. The larger surface area allows for a higher concentration of interfacial defects. Furthermore, smaller NCs are likely to form more fractile networks that lead to smaller domain sizes and/or discontinuing domains, narrowing the hysteresis loop. Although the net magnetic moment is larger in films prepared from benzyl alcohol-synthesized NCs, the retention of the tetragonal phase domains renders 0.4% Cr^{3+}:$BaTiO_3$ NCs synthesized in ethanol favorable building blocks for multiferroic structures and devices. The films prepared from water-synthesized NCs with similar doping concentrations did not show a detectable magnetic moment.

To confirm that the observed ferromagnetism arises from ordering of the dopant spins, we performed Cr $L_{2,3}$-edge XMCD measurements on the 0.4% Cr^{3+}:$BaTiO_3$ nanocrystalline film from Figure 10b, and the results are shown in Figure

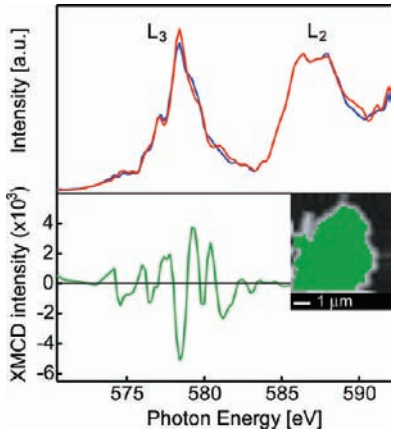

Figure 11. (top) Cr $L_{2,3}$-edge X-ray absorption spectra of a 0.4% Cr^{3+}:$BaTiO_3$ nanocrystalline film prepared from ethanol-synthesized NCs. The spectra were collected at 300 K using LCP (blue trace) and RCP (red trace) photons. (bottom) Cr L_3-edge XMCD spectrum obtained as the difference between the LCP and RCP spectra in the top part of the figure. Inset: STXM image of the sample corresponding to the absorption and XMCD spectra. The image was obtained using 598.2 eV photons, and the analyzed area is shown in green.

11. XMCD is defined as the difference in absorption of LCP (ρ^-) and RCP (ρ^+) photons in an external magnetic field.[57] The net magnetic moment of Cr^{3+} ions causes an imbalance of the spin-up and spin-down states in partially populated d orbitals that can be probed by the excitation of 2p core electrons to unfilled 3d states (L-edge absorption) using ρ^+ and ρ^- photons. XMCD therefore allows for element-specific detection of magnetic exchange interactions. STXM imaging enables XMCD measurements with high spatial resolution.[58] Figure 11 (top) shows Cr $L_{2,3}$-edge X-ray absorption spectra[59] collected at 300 K using LCP (blue trace) and RCP (red trace) X-ray beams. The sample area corresponding to the spectra is shown in the inset. Similar spectra were obtained from other parts of the sample, indicating a uniform distribution of Cr^{3+} dopants throughout the film. The LCP and RCP spectra are distinctly different in the L_3 region (i.e., peaks at 577.2 and 578.5 eV and shoulders at 579.4 and 581 eV), suggesting room-temperature magnetic exchange interactions of Cr^{3+} dopant ions.[60] The magnitude of the observed difference between the ρ^- and ρ^+ spectra in a small subsaturation magnetic field strongly suggests that the magnetic interactions involve long-range magnetic ordering,[61] consistent with the magnetization results in Figure 10b. The resulting XMCD spectrum is shown in Figure 11 (bottom). While a detailed analysis of this spectrum is beyond the scope of this work because of the small separation between the L_3 and L_2 edges caused by significant quantum-mechanical $j-j$ mixing in the case of light transition

dx.doi.org/10.1021/ja2091678 | J. Am. Chem.Soc. 2012, 134, 1136–1146

metals such as chromium,[62] this kind of spectral and spatial resolution will allow for future studies of the magnetic domain formation and quantitative determination of the magnetic interactions between the dopant ions and the $BaTiO_3$ NC host lattice.

CONCLUSIONS

We have demonstrated the solvent-controlled synthesis of Cr^{3+}:$BaTiO_3$ NCs having variable sizes and doping concentrations. A decrease in NC size and an increase in doping concentration favor the stabilization of paraelectric cubic $BaTiO_3$, with doping concentration being the dominant factor. Although the incorporation of dopant ions and a decrease in the NC size lead to a significant reduction of tetragonality, the Raman spectroscopy data indicate the retention of the local tetragonal phase in NCs that are ca. 7 nm in size and have a doping concentration of ca. 5%. The change of the host lattice symmetry by dopant incorporation or NC size significantly influences the electronic structure of the Cr^{3+} dopant ions, allowing for modulation of the functional properties of Cr^{3+}:$BaTiO_3$ NCs. Using NCs as precursors or building blocks for nanocrystalline films allows for the formation of the extended structural defects at the NC interfaces, which can mediate long-range magnetic ordering of Cr^{3+} ions substituted for Ti^{4+} sites. This approach, which was first applied to TCO NCs, has here been shown also to be applicable to dielectric oxides. The defect formation is correlated with a decrease in NC size due to an increase in surface-to-volume ratio. This trend is the opposite of that for the influence of NC size on the stabilization of the tetragonal ferroelectric phase, requiring an optimal balance between NC size and doping concentration to enable simultaneous retention of the ferroelectric phase and generation of the magnetic ordering. While the primary goal of this work was to establish the correlation between the NC size, structure, and interactions and the electronic structure and magnetic properties of Cr^{3+} dopant ions, the measurements of the electric polarization and the coupling between the electric dipole and magnetic moments remain an exciting topic for future studies. The main conclusion of this article is that a judicious choice of the synthesis conditions enables the simple preparation of complex perovskite-type NCs that can be used for the bottom-up formation of multiferroic or other multifunctional materials and devices.

ASSOCIATED CONTENT

Supporting Information

Unit cell structure of tetragonal $BaTiO_3$, SEM image of water-synthesized $BaTiO_3$ NCs, XRD patterns of Cr^{3+}:$BaTiO_3$ NCs synthesized in ethanol and benzyl alcohol, Raman spectra of undoped and Cr^{3+}-doped $BaTiO_3$ NCs, electronic absorption and MCD spectra of Cr^{3+}:$BaTiO_3$ NCs, magnetization data for free-standing Cr^{3+}:$BaTiO_3$ NCs, and complete refs 3 and 24a. This material is available free of charge via the Internet at http://pubs.acs.org.

AUTHOR INFORMATION

Corresponding Author

pavler@uwaterloo.ca

ACKNOWLEDGMENTS

This work was funded by NSERC (Discovery and RTI Grants), the Canada Foundation for Innovation (CFI-LOF 204782), and the Ontario Research Fund (ORF-RI 204782). P.V.R. thanks the Canada Research Chairs Program (NSERC) and the Ontario Ministry of Research and Innovation (Early Researcher Award) for partial support of this work. M.H. acknowledges the Canadian Light Source (CLS) for a Graduate Travel Support Award. The research described in this article was partly performed at CLS, which is supported by NSERC, NRC, CIHR, the Province of Saskatchewan, Western Economic Diversification Canada, and the University of Saskatchewan. TEM measurements were performed at the Canadian Center for Electron Microscopy in the Brockhouse Institute for Materials Research at McMaster University. We thank Dr. Jian Wang (CLS) for assistance with the STXM measurements at beamline 10ID-1.

REFERENCES

(1) (a) Fiebeig, M. *J. Phys. D: Appl. Phys.* **2005**, *38*, R123–R152. (b) Wang, K. F.; Liu, J.-M.; Ren, Z. F. *Adv. Phys.* **2009**, *58*, 321–448.
(2) Hill, N. A. *J. Phys. Chem. B* **2000**, *104*, 6694–6709.
(3) Zheng, H.; et al. *Science* **2004**, *303*, 661–663.
(4) (a) Lottermoser, T.; Lonkai, T.; Amann, U.; Hohlwein, D.; Ihringer, J.; Fiebeig, M. *Nature* **2004**, *430*, 541–544. (b) Zavaliche, F.; Zhao, T.; Zheng, H.; Straub, F.; Cruz, M. P.; Yang, P.-L.; Hao, D.; Ramesh, R. *Nano Lett.* **2007**, *7*, 1586–1590.
(5) (a) Zhao, T.; Scholl, A.; Zavaliche, F.; Lee, K.; Barry, M.; Doran, A.; Cruz, M. P.; Chu, Y. H.; Ederer, C.; Spaldin, N. A.; Das, R. R.; Kim, D. M.; Baek, S. H.; Eom, C. B.; Ramesh, R. *Nat. Mater.* **2006**, *5*, 823–829. (b) Cheong, S.-W.; Mostovoy, M. *Nat. Mater.* **2007**, *6*, 13–20. (c) Hemberger, J.; Lunkenheimer, P.; Fichtl, R.; Krug von Nidda, H.-A.; Tsurkan, V.; Loidl, A. *Nature* **2005**, *434*, 364–367. (d) Jo, Y.; Jang, K.-H.; Park, J.-G.; Kim, H. C.; Kim, T. H.; Kim, K. H.; Hur, N.; Park, S.; Cheong, S.-W. *Phys. Rev. B* **2007**, *76*, No. 012406.
(6) Lines, M. E.; Glass, A. M. *Principles and Applications of Ferroelectrics and Related Materials*; Clarendon Press: Oxford, U.K., 1977.
(7) Merz, W. J. *Phys. Rev.* **1954**, *95*, 690–698.
(8) Bruno, S. A.; Swanson, D. K.; Burn, I. *J. Am. Ceram. Soc.* **1993**, *76*, 1233–1241.
(9) Park, B. H.; Kang, B. S.; Bu, S. D.; Noh, T. W.; Lee, J.; Jo, W. *Nature* **1999**, *401*, 682–684.
(10) Huybrechts, B.; Ishizaki, K.; Takata, M. *J. Mater. Sci.* **1995**, *30*, 2463–2474.
(11) (a) Glass, A. M. *Science* **1987**, *235*, 1003–1009. (b) Gill, D. M.; Conrad, C. W.; Ford, G.; Wessels, B. W.; Ho, S. T. *Appl. Phys. Lett.* **1997**, *71*, 1783–1785.
(12) Yu, J.; Chu, J. *Encycl. Nanosci. Nanotechnol.* **2004**, *6*, 389–416.
(13) Strukov, B. A.; Levanyuk, A. P. *Ferroelectric Phenomena in Crystals: Physical Foundations*; Springer: Berlin, 1998.
(14) Shannon, R. D. *Acta Crystallogr.* **1976**, *A32*, 751–767.
(15) Xu, Y. *Ferroelectric Materials and Their Applications*; North-Holland: Amsterdam, 1991.
(16) Wada, S.; Suzuki, T.; Osada, M.; Kakihana, M.; Noma, T. *Jpn. J. Appl. Phys., Part 1* **1998**, *37*, 5385–5393.
(17) Noma, T.; Wada, S.; Yano, M.; Suzuki, T. *J. Appl. Phys.* **1996**, *80*, 5223–5233.
(18) Blinc, R. *Struct. Bonding (Berlin)* **2007**, *124*, 51–67.
(19) Sedykh, P.; Michel, D. *Phys. Rev. B* **2009**, *79*, No. 134119.
(20) Sun, W. *J. Appl. Phys.* **2006**, *100*, No. 083503.
(21) Smith, M. B.; Page, K.; Siegrist, T.; Redmond, P. L.; Walter, E. C.; Seshadri, R.; Brus, L. E.; Steigerwald, M. L. *J. Am. Chem. Soc.* **2008**, *130*, 6955–6963.
(22) Uchino, K.; Sadanaga, E.; Hirose, T. *J. Am. Ceram. Soc.* **1989**, *72*, 1555–1558.
(23) Yamamoto, T.; Niori, H.; Moriwake, H. *Jpn. J. Appl. Phys., Part 1* **2000**, *39*, 5683–5686.
(24) (a) Tenne, D. A.; et al. *Science* **2006**, *313*, 1614–1616. (b) Naumov, I. I.; Bellaiche, L.; Fu, H. *Nature* **2004**, *423*, 737–740.

(c) Ahn, C. H.; Rabe, K. M.; Triscone, J.-M. *Science* **2004**, *303*, 488−491.
(25) (a) Khatib, D.; Kinase, W.; Lifsal, L.; Toumanari, A.; Bougarfa, L.; Beaucamps, Y. *Ferroelectr., Lett. Sect.* **1994**, *18*, 121−125. (b) Zhang, J.; Yin, Z.; Zhang, M.-S.; Scott, J. F. *Solid State Commun.* **2001**, *118*, 241−246.
(26) (a) Farvid, S. S.; Dave, N.; Wang, T.; Radovanovic, P. V. *J. Phys. Chem. C* **2009**, *113*, 15928−15933. (b) Farvid, S. S.; Dave, N.; Radovanovic, P. V. *Chem. Mater.* **2010**, *22*, 9−11. (c) Wang, T.; Radovanovic, P. V. *J. Phys. Chem. C* **2011**, *115*, 406−413. (d) Wang, T.; Farvid, S. S.; Abulikemu, M.; Radovanovic, P. V. *J. Am. Chem. Soc.* **2010**, *132*, 9250−9252.
(27) Radovanovic, P. V.; Gamelin, D. R. *Phys. Rev. Lett.* **2003**, *91*, No. 157202.
(28) Farvid, S. S.; Ju, L.; Worden, M.; Radovanovic, P. V. *J. Phys. Chem. C* **2008**, *112*, 17755−17759.
(29) Farvid, S. S.; Wang, T.; Radovanovic, P. V. *Proc. SPIE* **2010**, *7760*, 77600B.
(30) Lever, A. B. P. *Inorganic Electronic Spectroscopy*, 2nd ed.; Elsevier: Amsterdam, 1984.
(31) Niederberger, M.; Garnweitner, G.; Pinna, N.; Antonietti, M. *J. Am. Chem. Soc.* **2004**, *126*, 9120−9126.
(32) Dave, N.; Pautler, B. G.; Farvid, S. S.; Radovanovic, P. V. *Nanotechnology* **2010**, *21*, No. 134023.
(33) (a) Tripathy, S. S.; Raichur, A. M. *J. Dispersion Sci. Technol.* **2008**, *29*, 230−239. (b) Rai, P. B.; Sathish, P.; Krishnamurty, S. *Ferroelectrics* **2004**, *306*, 195−208.
(34) Niederberger, M. *Acc. Chem. Res.* **2007**, *40*, 793−800.
(35) Kolen'ko, Y. V.; Kovnir, K. A.; Neira, I. S.; Taniguchi, T.; Ishigaki, T.; Watanabe, T.; Sakamoto, N.; Yoshimura, M. *J. Phys. Chem. C* **2007**, *111*, 7306−7318.
(36) Wei, X.; Xu, G.; Ren, Z.; Wang, Y.; Shen, G.; Han, G. *J. Am. Ceram. Soc.* **2008**, *91*, 315−318.
(37) Wei, X.; Xu, G.; Ren, Z.; Wang, Y.; Shen, G.; Han, G. *Mater. Lett.* **2008**, *62*, 3666−3669.
(38) Kwon, S.-G.; Park, B.-H.; Choi, K.; Choi, E.-S.; Nam, S.; Kim, J.-W.; Kim, J.-H. *J. Eur. Ceram. Soc.* **2006**, *26*, 1401−1404.
(39) Shiratori, Y.; Pithan, C.; Dornseiffer, J.; Waser, R. *J. Raman Spectrosc.* **2007**, *38*, 1288−1299.
(40) Page, K.; Proffen, T.; Niederberger, M.; Seshadri, R. *Chem. Mater.* **2010**, *22*, 4386−4391.
(41) Li, G.; Boerio-Goates, J.; Woodfield, B. F.; Li, L. *Appl. Phys. Lett.* **2004**, *85*, 2059−2061.
(42) Ishikawa, K.; Uemori, T. *Phys. Rev. B* **1999**, *60*, 11841−11845.
(43) Tsunekawa, S.; Ito, S.; Mori, T.; Ishikawa, K.; Li, Z.-Q.; Kawazoe, Y. *Phys. Rev. B* **2000**, *62*, 3065−3070.
(44) Perebeinos, V.; Chan, S.-W.; Zhang, F. *Solid State Commun.* **2002**, *123*, 295−297.
(45) Hoshina, T.; Kakemoto, H.; Tsurumi, T.; Wada, S.; Yashima, M. *J. Appl. Phys.* **2006**, *99*, No. 054311.
(46) El Marssi, M.; Le Marrec, F.; Lukyanchuk, I. A.; Karkut, M. G. *J. Appl. Phys.* **2003**, *94*, 3307−3312.
(47) Venkateswaran, U. D.; Naik, V. M.; Naik, R. *Phys. Rev. B* **1998**, *58*, 14256−14260.
(48) Huang, T.-C.; Wang, M.-T.; Sheu, H.-S.; Hsieh, W.-F. *J. Phys.: Condens. Matter* **2007**, *19*, No. 476212.
(49) Hong, J.; Fang, D. *Appl. Phys. Lett.* **2008**, *92*, No. 012906.
(50) Buscaglia, M. T.; Buscaglia, V.; Viviani, M. *J. Am. Ceram. Soc.* **2001**, *84*, 376−384.
(51) Dutta, P. K.; Gallagher, P. K.; Twu, J. *Chem. Mater.* **1993**, *5*, 1739−1743.
(52) The water-synthesized NCs were only partly dispersable because of the large NC sizes. The colloidal suspensions were not sufficiently transparent to obtain clear absorption spectra in solution.
(53) Piepho, S. B.; Schatz, P. N. *Group Theory in Spectroscopy with Applications to Magnetic Circular Dichroism*; Wiley: New York, 1983.
(54) Muller, K. A.; Berlinger, W.; Albers, J. *Phys. Rev. B* **1985**, *32*, 5837−5844.
(55) Archer, P. I.; Radovanovic, P. V.; Heald, S. M.; Gamelin, D. R. *J. Am. Chem. Soc.* **2005**, *127*, 14479−14487.
(56) Kaspar, T. C.; Heald, S. M.; Wang, C. M.; Bryan, J. D.; Droubay, T.; Shutthanandan, V.; Thevuthasan, S.; McCready, D. E.; Kellock, A. J.; Gamelin, D. R.; Chambers, S. A. *Phys. Rev. Lett.* **2005**, *95*, No. 217203.
(57) Stohr, J. *J. Magn. Magn. Mater.* **1999**, *200*, 470−497.
(58) Stohr, J.; Anders, S. *IBM J. Res. Dev.* **2000**, *44*, 535−551.
(59) Corradini, V.; Moro, F.; Biagi, R.; del Pennino, U.; De Renzi, V.; Carretta, S.; Santini, P.; Affronte, M.; Cezar, J. C.; Timco, G.; Winpenny, R. E. P. *Phys. Rev. B* **2008**, *77*, No. 014402.
(60) Wu, N.; He, X.; Wysocki, A. L.; Lanke, U.; Komesu, T.; Belashchenko, K. D.; Binek, C.; Dowben, P. A. *Phys. Rev. Lett.* **2011**, *106*, No. 087202.
(61) Hegde, M.; Farvid, S. S.; Hosein, I. D.; Radovanovic, P. V. *ACS Nano* **2011**, *5*, 6365−6373.
(62) Goering, E. *Philos. Mag.* **2005**, *85*, 2895−2911.